

A Ramsey Ion Gradiometer for Single-Molecule State Detection

Sean D. Huver

NVIDIA

(Dated: August 19, 2025)

Abstract

The characterization of ligand–receptor interactions is a cornerstone of modern pharmacology; however, current methods are hampered by limitations such as ensemble averaging and invasive labeling. We propose a theoretical quantum sensing solution, the Quantum Ligand-Binding Interrogator (QLI), designed to overcome these challenges. The QLI is a differential sensor, or gradiometer, that uses a pair of co-trapped atomic ions to perform label-free detection of the electric field gradient produced by a single ligand binding to its receptor in vitrified samples. This gradiometric approach provides robust common-mode rejection of background electric field noise. To bridge the gap between the cryogenic, ultra-high-vacuum environment required for the sensor and the biological sample, we propose an architecture based on a vitrified sample mounted on a scanning probe. This enables the detection of the electrostatic signature of a single molecule in a specific conformational state (e.g., bound vs. unbound). This paper details the conceptual framework of the QLI, the experimental architecture, the measurement protocol using entangled two-ion spin states, and an analysis of key engineering risks. Anchoring to state-of-the-art single-ion low-frequency sensitivities (sub-mV m⁻¹ / $\sqrt{\text{Hz}}$), we project SNR = 1 in tens of seconds at a 10 μm ion–sample separation for $\Delta p \sim 20 \text{ D}$, with feasibility dominated by the (as yet unmeasured) electrostatic stability of vitrified samples. If realized, QLI would provide direct single-molecule measurements of binding-induced electric field changes, offering a new path for experimental validation of computational models of drug–receptor interactions.

I. INTRODUCTION

The interaction between a ligand and its receptor is a fundamental event underpinning nearly all cell signaling and modern pharmacology [1]. Accurately characterizing these interactions at the single-molecule level is crucial for understanding biological mechanisms, as ensemble averaging obscures stochastic behaviors and transient states. Yet, current single-molecule methods suffer from significant limitations.

Techniques relying on fluorescent labeling, such as single-molecule Förster Resonance Energy Transfer (smFRET), are powerful but invasive. The attachment of fluorophores can alter binding affinity and conformational dynamics; studies have shown perturbations in dissociation constants (K_D) by one to two orders of magnitude depending on label placement

and type [2, 3]. Furthermore, phototoxicity and photobleaching inherently limit observation times and can damage the biological system [4]. Label-free methods like Surface Plasmon Resonance (SPR) typically require ensemble averaging and often lack the sensitivity to detect small molecule interactions (e.g., < 300 Da) [5].

This creates a measurement gap for a specific class of biological questions where the electrostatic environment is paramount and any molecular label is unacceptably perturbative. For example, in the study of metalloenzymes, ion channels, or allosteric regulation, the precise arrangement and strength of the local electric field dictates function. While techniques such as vibrational Stark effect spectroscopy can probe electric fields in biological systems, they operate on ensemble samples and cannot resolve single-molecule heterogeneity [6]. Scanning probe methods with functionalized tips can achieve single-molecule resolution but cannot directly quantify electric field magnitudes [7]. Moreover, the computational methods used to predict these interactions (e.g., molecular dynamics with Poisson–Boltzmann solvers) produce electric field maps that differ by factors of 2–10 depending on the force field and solvation model employed, yet lack direct experimental validation at the single-molecule scale [8, 9]. There is a need for a method that can provide a “ground truth” electrostatic measurement of a binding event—even if limited to static, vitrified states—serving as a benchmark for theory and revealing aspects of molecular recognition invisible to other techniques.

To achieve the sensitivity required for single-molecule electric field detection, we look beyond conventional biophysical methods to emerging quantum technologies. The pursuit of high-precision measurements has driven the rapid development of quantum sensing, which exploits quantum coherence and entanglement to surpass classical measurement limits [10]. Trapped atomic ions, renowned for their use in atomic clocks [11], have emerged as exceptionally sensitive electrometers capable of detecting fields as weak as $mV/m/\sqrt{Hz}$ [12]. Their extraordinary sensitivity arises from perfect isolation in ultra-high vacuum, precise quantum state control via laser manipulation, and the ability to exploit quantum entanglement between multiple ions for enhanced measurement precision [13, 14]. While quantum sensors such as nitrogen-vacancy centers have been successfully applied to biological systems at room temperature [15], trapped ions offer superior sensitivity and quantum control at the cost of requiring cryogenic, vacuum conditions—a trade-off we address through sample vitrification.

This paper proposes the Quantum Ligand-Binding Interrogator (QLI), a novel application

of trapped-ion quantum sensing designed to address this specific measurement challenge. The QLI architecture is based on a two-ion electric field gradiometer operating in a cryogenic environment. By measuring the *difference* in the electric field experienced by two closely spaced ions, the system can reject common-mode background noise while remaining sensitive to the strong local field gradient produced by a nearby ligand-binding event. To bridge the environmental gap between the sensor and the sample, we propose an architecture using a vitrified (flash-frozen) biological sample mounted on a scanning probe. The QLI offers a pathway to a new benchmark tool in biophysics and drug discovery [16].

II. THE QUANTUM LIGAND-BINDING INTERROGATOR (QLI)

A. Conceptual Framework and Positioning

The QLI is designed to detect the change in the local electrostatic environment upon ligand binding. This measurement avoids fluorescent labels and operates through long-range electrostatic sensing, though it requires vitrification which captures only static conformational states.

a. Cost-benefit analysis and use cases. It is important to contextualize the QLI within the existing landscape of biophysical tools (Table I). The QLI is characterized by high technical complexity, significant infrastructure requirements (cryogenic UHV), and inherently low throughput (see Sec. III). It is not intended as a replacement for high-throughput screening methods like SPR, nor can it capture real-time dynamics like smFRET. Instead, QLI is designed as a specialized, high-fidelity instrument for answering questions where existing methods fail: the direct, label-free measurement of the electrostatic signature of a single molecule in a defined state. The primary use case is establishing “ground truth” benchmarks for computational electrostatics. In scenarios where the perturbation from a fluorescent label is unacceptable (e.g., studying ion channel gating mechanisms or metalloenzyme active sites), the investment in QLI’s complexity could be justified by the unique information it provides.

B. The Gradiometer Principle and Geometry

A primary challenge in sensitive electrometry is that a single-ion sensor is sensitive to *all* electric fields, including large, slowly drifting stray fields from patch potentials on the trap electrodes [13]. These background fields can exceed the target signal by many orders of magnitude.

To overcome this, the QLI is designed as a differential sensor, or gradiometer, using two co-trapped ions. The electric field from the nearby ligand binding event has a strong gradient ($E \propto 1/r^3$ for a dipole), creating a large differential signal between the two ions [17]. In contrast, the background field from distant sources is nearly uniform across the ions' small separation (d) and is rejected as common-mode noise [13, 18].

a. Coordinate conventions and explicit geometry. We define the geometry as illustrated in Fig. 1. We take \hat{z} as the surface normal of the sample/stylus (sample near $z=0$). The two ions are confined along the trap axis, defined as \hat{x} . In the surface-trap implementation used here, the ions share the same height h above the sample and are separated laterally by d . The ion positions are therefore $\mathbf{r}_{S/R} = (\pm d/2, 0, h)$.

TABLE I. Comparison with competing single-molecule techniques.

Technique	Label needed?	Sensitivity	Information content	Key limitation
QLI (Proposed)	No	Single molecule	Static electrostatic field map; benchmark for computation	Technical complexity; sample; low throughput
smFRET	Yes	Single molecule	Conformational dynamics; distance	Photobleaching; label perturbation [4]
SPR	No	Ensemble (typically)	Binding kinetics ($k_{\text{on}}/k_{\text{off}}$)	Low sensitivity for small molecules [5]
Nanopore sensing	No	Single molecule	Translocation dynamics; structure	Controlling translocation speed

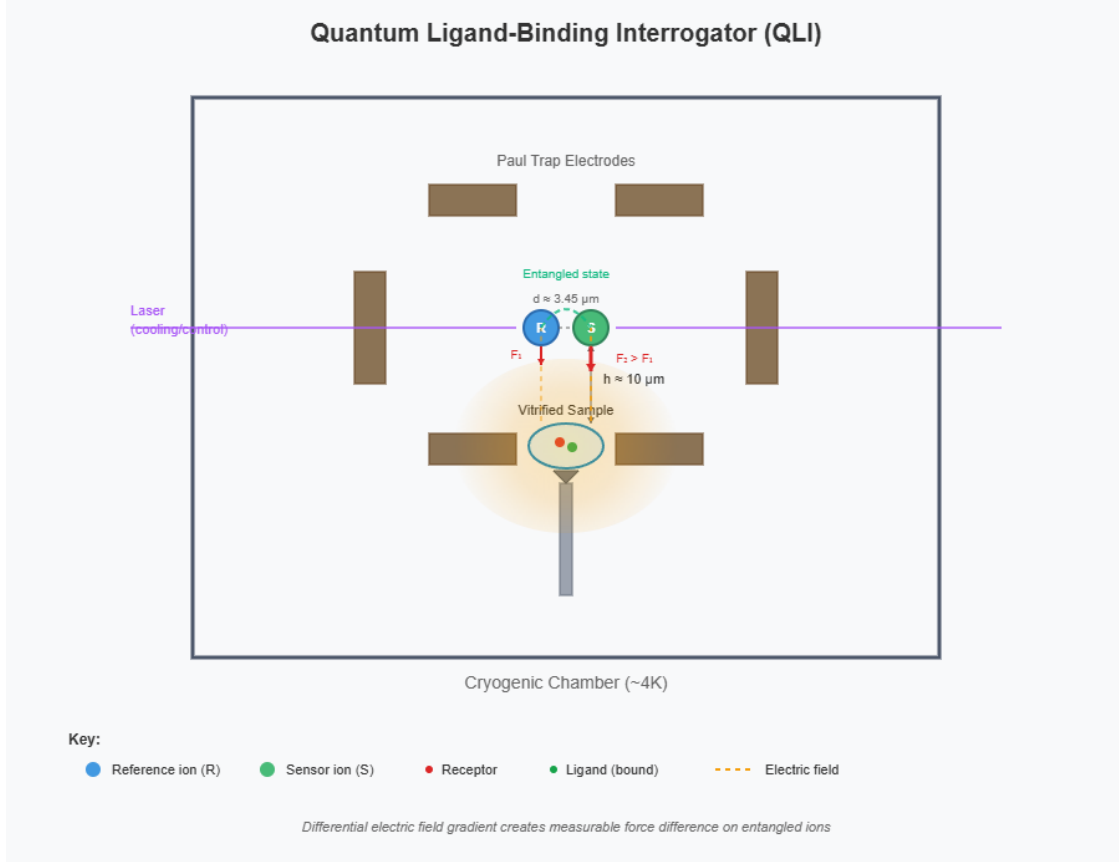


FIG. 1. Conceptual design of the Quantum Ligand-Binding Interrogator (QLI). A two-ion crystal (sensor S, reference R) is confined in a cryogenic Paul trap. A vitrified biological sample is mounted on a stylus and positioned near the ions. A binding-induced dipole change normal to the surface produces a *lateral* differential field ΔE_x across the ions, which drives the axial stretch mode and is read out via an entangled two-ion sequence.

The gradiometer measures the *lateral* differential field along the trap axis: $\Delta E_x \equiv E_x(+d/2, h) - E_x(-d/2, h)$.

For a binding-induced dipole change $\Delta \mathbf{p} = \Delta p \hat{z}$ in the sample (normal to the surface), the free-space lateral differential field is

$$\Delta E_x(h, d; \Delta p) = \frac{\Delta p}{4\pi\epsilon_0} \frac{3hd}{(h^2 + (d/2)^2)^{5/2}} = \frac{\Delta p}{4\pi\epsilon_0} d h^{-4} c_{\text{eff}}\left(\frac{d}{h}\right), \quad (1)$$

$$c_{\text{eff}}(u) \equiv \frac{3}{(1 + (u/2)^2)^{5/2}}, \quad c_{\text{eff}}(0) = 3, \quad c_{\text{eff}}(0.345) \approx 2.79. \quad (2)$$

b. Electromagnetic modeling and interface effects. The presence of the dielectric medium modifies the electric field reaching the ions. In our baseline analysis, we approx-

imate this effect using the idealized model of a dipole embedded in a semi-infinite planar dielectric (amorphous ice, $\epsilon_r \approx 3$) interfacing with vacuum. This leads to a multiplicative transmission factor for the normal-dipole contribution, $\eta_{\perp} \simeq 2/(\epsilon_r+1) \approx 0.5$.

This planar model is an acknowledged simplification used to establish baseline feasibility. It neglects the realistic experimental geometry, including: (a) the finite thickness of the vitrified film (t); (b) the curvature of the stylus apex (radius R); (c) multiple dielectric interfaces (e.g., vacuum/ice/quartz); and (d) the influence of nearby trap electrodes.

We argue that this simplification is appropriate for the current feasibility assessment for the following reasons:

1. **Robustness of h^{-4} scaling:** The steep h^{-4} scaling (Eq. 1) arises from the differential measurement of a localized dipolar source ($E \propto 1/r^3$). This scaling behavior is robust provided the measurement occurs in the far field relative to the source dimensions, i.e., $h \gg R$ and $h \gg t$. For a target $h = 10 \mu\text{m}$ and typical stylus parameters ($R \lesssim 1 \mu\text{m}, t < 1 \mu\text{m}$), this condition is satisfied. The dielectric environment modifies the magnitude of the effective dipole moment seen in the vacuum, but it does not alter the fundamental far-field spatial dependence.
2. **Conservative estimate of magnitude:** The primary uncertainty lies in the prefactor η . The factor $\eta \approx 0.5$ represents the suppression of the electric field due to the polarization of the bulk dielectric medium. In the case of a finite, thin film with curvature, the volume of polarizable material is reduced compared to a bulk medium. Therefore, the actual transmission factor is likely bounded between the bulk case ($\eta \approx 0.5$) and the vacuum case ($\eta = 1$). By adopting the lower bound, we ensure our feasibility estimates (Sec. III) are conservative.
3. **Modeling and calibration plan:** While the idealized model is sufficient for initial feasibility, detailed numerical electromagnetic simulations (e.g., finite element or boundary element) will be essential during the engineering phase to accurately model the specific geometry. Furthermore, the realized QLI will require *in situ* calibration. This will involve (i) measuring the distance dependence (sweeping h) to confirm the h^{-4} scaling, and (ii) using a calibrated source (e.g., a metallic nano-tip with an applied voltage, Milestone 1) to determine the effective geometric factor η_{eff} of the specific experimental configuration.

C. Sensing Protocol and State Evolution

The measurement protocol utilizes Ramsey interferometry enhanced by spin-dependent forces (SDF) to transduce the electric field gradient into a measurable spin-state population. This requires coupling the motion of the ions, which is affected by the external electric field, to their internal spin states. Let the two internal spin states of each ion be $|\downarrow\rangle$ and $|\uparrow\rangle$.

Crucially, the electric field gradient exerts a differential force on the two ions. This differential force couples specifically to the axial stretch mode (out-of-phase motion) of the two-ion crystal, while uniform fields couple to the center-of-mass mode. We denote the state of the axial stretch mode as $|n\rangle$.

The protocol proceeds as follows:

1. **Initialization:** The two ions are prepared in a known internal ground state and the axial stretch mode is cooled near its motional ground state, $|\psi_0\rangle = |\downarrow\downarrow\rangle|0\rangle$.
2. **Entangled state preparation:** A Mølmer–Sørensen gate, \hat{U}_{MS} , creates an entangled Bell state [19], $|\psi_1\rangle = \hat{U}_{\text{MS}}|\psi_0\rangle = \frac{1}{\sqrt{2}}(|\uparrow\downarrow\rangle + |\downarrow\uparrow\rangle)|0\rangle$. This state is inherently sensitive to differential forces and resides in a decoherence-free subspace (DFS) regarding common-mode magnetic field noise [20, 21].
3. **Interrogation via multi-loop SDF:** A sequence of spin-dependent optical dipole forces is applied, tuned near the frequency of the stretch mode. This entangles the spin and motional states, causing the stretch mode to be displaced into a coherent state $|\alpha(t)\rangle$ conditionally on the two-qubit spin state [22]. The external differential force from the ligand, $F_{\text{diff}} = e \cdot \Delta E_x$, perturbs these phase-space trajectories. The SDF sequence is designed as a series of closed loops in phase space (a spin-echo sequence) to enhance robustness and ensure the motion and spin disentangle at the end of the total interrogation time, T .

The perturbation from the ligand's field results in an accumulated differential geometric phase, ϕ , between the two spin components, $|\psi_2\rangle = \frac{1}{\sqrt{2}}(|\uparrow\downarrow\rangle + e^{i\phi}|\downarrow\uparrow\rangle)|0\rangle$.

a. Field-to-phase transduction (closed SDF loops). With a near-resonant SDF on the stretch mode (detuning δ) and differential spin operator \hat{s} , the interaction Hamil-

tonians are

$$H_{\text{SDF}}(t) = \hbar g(a e^{i\delta t} + a^\dagger e^{-i\delta t}) \hat{s}, \quad H_{\text{ext}} = \frac{e \Delta E_x}{\sqrt{2}} x_0 (a + a^\dagger). \quad (3)$$

A second-order Magnus expansion yields a relative phase between $|\uparrow\downarrow\rangle$ and $|\downarrow\uparrow\rangle$,

$$\phi = \mathcal{G}_E(g, \delta, T) \Delta E_x, \quad (4)$$

$$\mathcal{G}_E(g, \delta, T) = \frac{\sqrt{2} e g x_0}{\hbar} \left(\frac{\sin \delta T}{\delta^2} - \frac{T \cos \delta T}{\delta} \right) \xrightarrow{\delta T = 2\pi N} \frac{2\pi N \sqrt{2} e g x_0}{\hbar \delta^2}, \quad (5)$$

where \mathcal{G}_E is the transduction gain of the sequence, which depends on the experimental parameters of the SDF loops [14, 23]. The condition $\delta T = 2\pi N$ enforces loop closure (spin-motion disentanglement). Thus a *static* ΔE_x produces a nonzero phase that accumulates linearly with the number of loops N . Small closure errors ε ($\delta T = 2\pi N + \varepsilon$) leave \mathcal{G}_E unchanged to first order but reduce contrast by $\exp[-(2\bar{n}+1)(g\varepsilon/\delta)^2]$.

4. **Analysis pulse and measurement:** To read out the phase, the entanglement operation is reversed. An analysis pulse, $\hat{U}_{\text{analysis}} = \hat{U}_{\text{MS}}^\dagger$, converts the phase ϕ into a population difference, $|\psi_3\rangle = \hat{U}_{\text{MS}}^\dagger |\psi_2\rangle = \cos(\phi/2) |\downarrow\downarrow\rangle - i \sin(\phi/2) |\uparrow\uparrow\rangle$. The population in the bright state, $P_{\downarrow\downarrow} = \cos^2(\phi/2)$, is measured via state-dependent fluorescence. After M repetitions, the phase uncertainty is $\Delta\phi \simeq 1/\sqrt{M}$, consistent with the standard quantum limit [24].

D. Proposed Physical Implementation

The practical implementation of this protocol requires a synthesis of state-of-the-art techniques from quantum sensing, cryogenics, and nanotechnology.

Two-ion gradiometer: A two-ion crystal of $^{171}\text{Yb}^+$ will be confined in a cryogenic linear Paul trap cooled to ~ 4 K to reduce intrinsic electric field noise from the trap electrodes [13]. A third ion of a different species (e.g., $^{40}\text{Ca}^+$) will be co-trapped to sympathetically recoil the motional modes between experimental shots, preventing cumulative heating.

Bio-interface and sample preparation: To bridge the UHV/cryogenic environment of the sensor with the biological sample, we will use a vacuum-compatible, vitrified sample. A single receptor molecule is anchored to the apex of an AFM-style quartz stylus, plunge-frozen, and transferred under vacuum into the cryogenic chamber. This approach, central to cryo-EM [25], preserves the molecular structure in a native-like state.

Complement to kinetic measurements: This method is designed to provide high-fidelity electrostatic snapshots of static conformational states (e.g., apo vs. holo). It is therefore a complementary tool to, not a replacement for, dynamic methods like SPR. The binding interaction is studied by comparing measurements from two sample preparations: one vitrified in the unbound state and one vitrified in the ligand-bound state.

Ion–molecule positioning: The sample-mounted stylus will be positioned to achieve a target stand-off distance of $h \approx 10 \mu\text{m}$. While state-of-the-art stylus traps currently operate at $\sim 30 \mu\text{m}$, achieving $10 \mu\text{m}$ is a credible near-term R&D goal and represents a key engineering objective for this project [26, 27].

E. Averaging Strategy and Coherence Maintenance

Multi-minute integrations do not require a single quantum superposition to persist for minutes. Instead, we perform M repeated, short coherent interrogations (“shots”) of duration T_{live} (typically 10^2 – 10^3 ms under dynamical decoupling), separated by overhead T_{dead} for cooling, state prep, and readout. Each shot uses a phase-sensitive control sequence (echo/XY8/quantum lock-in) whose toggling function $y(t)$ defines a reference band around f_0 (e.g. 5.8 Hz).

Let S be the noise-equivalent field sensitivity ($\text{V m}^{-1}/\sqrt{\text{Hz}}$) of the chosen protocol (e.g., $S_{\text{AC}} = 0.96 \text{ mV m}^{-1}/\sqrt{\text{Hz}}$, $S_{\text{DC}} = 1.97 \text{ mV m}^{-1}/\sqrt{\text{Hz}}$ [28]). For a total wall-clock time $T_{\text{tot}} = M(T_{\text{live}} + T_{\text{dead}})$, the duty cycle is $D = T_{\text{live}}/(T_{\text{live}} + T_{\text{dead}})$ and the signal-to-noise scales as

$$\text{SNR}(T_{\text{tot}}) = \frac{\Delta E}{S} \sqrt{T_{\text{live}} M} = \frac{\Delta E}{S} \sqrt{D T_{\text{tot}}}, \quad (6)$$

i.e. exactly the $\propto \sqrt{\text{time}}$ behavior quoted in our feasibility tables. Crucially, the quantum coherence only needs to survive during T_{live} for each shot—not for the entire T_{tot} .

a. Keeping per-shot coherence high. We use standard tools to make T_{live} long compared to the inverse of the demodulation frequency f_0 :

- **Clock states / DFS:** Encode in magnetically insensitive hyperfine states or a two-ion decoherence-free subspace to suppress common-mode B -field noise.
- **Dynamical decoupling / quantum lock-in:** Echo/XY8- n or spin-lock sequences implement a narrowband filter function $|Y(\omega)|^2$ centered at $2\pi f_0$, extending T_2 into

the 10^2 – 10^3 ms range while rejecting $1/f$ noise [29, 30].

- **Magnetic quieting:** μ -metal shielding, stable current supplies, and (optional) active field stabilization maintain a quiet DC environment; common lasers and LOs drive both ions to suppress relative phase noise.
- **Motional hygiene:** Sympathetic cooling between shots resets the stretch/COM modes; SDF loops are designed to close in phase space so spin and motion disentangle at the end of each shot.
- **Photocharging control:** Beam geometry and baffles minimize scatter onto the vitrified stylus; if needed, microwave-based gates avoid optical charging (see Sec. III).

b. Phase coherence across shots is classical. The phase reference for the measurement is derived from a stable classical oscillator (e.g., the laser local oscillator or the timing system controlling the pulse sequence). The demodulation reference (the sign pattern of the toggling function $y(t)$, or a small, known stylus dither at f_0) is phase-stable from the same timebase each shot. The field estimate from each shot is demodulated against this *same* classical reference and then averaged. We multiply each shot’s outcome by this known reference sign and average; this is coherent *classical* integration of the estimate, not quantum phase storage between shots. The phase of the quantum state is measured and recorded classically during readout; this classical record is then averaged coherently over M shots. Slow drifts are suppressed by phase-cycling ($y \rightarrow -y$) and by pairing shots with opposite demodulation sign.

c. Practical numbers. The optimal live time for the $f_0 \approx 5.8$ Hz protocol is $T_{\text{live}} \approx 1/f_0 \simeq 172$ ms (as in [28]). With a conservative duty cycle $D = 0.5$ – 0.8 , achieving $\text{SNR} = 1$ in ~ 40 s (AC, $h = 10$ μm) corresponds to $M \sim 200$ – 400 shots—each maintaining coherence for < 1 s, never minutes. Longer wall-clock averages simply increase M .

III. FEASIBILITY AND RISK ANALYSIS

The realization of the QLI hinges on achieving sufficient signal-to-noise ratio (SNR) in a complex experimental environment. This requires minimizing the ion–molecule separation, maximizing the intrinsic sensitivity of the sensor, and understanding the noise characteristics of the biological sample itself.

A. Ion–Molecule Separation and Trap Geometry

The target ion–surface separation of $h = 10 \mu\text{m}$ is a critical engineering goal, as the signal strength scales nominally as h^{-4} . While state-of-the-art stylus traps currently operate near $30 \mu\text{m}$ with low motional heating rates at 4 K, pushing towards $10 \mu\text{m}$ is an active area of research [26, 27]. A key challenge at these small separations is the risk of laser-induced photo-charging. Scattered laser light striking the dielectric stylus tip can cause it to accumulate charge, creating a large, unstable source of electric field noise. Mitigation of this risk is critical and may involve integrating shielding baffles into the trap structure, optimizing the optical path to minimize scatter onto the stylus, or potentially developing measurement schemes that rely on microwave radiation instead of lasers for the entangling gate operations.

B. Signal Strength Analysis

We estimate the expected signal based on the change in the electric dipole moment upon binding, Δp . In this context Δp is the *net change* in the permanent dipole of the receptor–ligand complex (including local side-chain rearrangements and bound-water reorientation) between the apo and holo states; it is the quantity that enters the far-field dipolar term. As a physically transparent scale, moving a charge q over a distance ℓ produces $p = q\ell$, so in Debye units

$$\Delta p [\text{D}] \approx 4.80 \times (q/e) \times \ell [\text{\AA}], \quad (7)$$

i.e. a single elementary charge displaced by 4\AA corresponds to $\sim 19 \text{ D}$, and by 5\AA to $\sim 24 \text{ D}$. Binding pockets routinely reorganize fractional and integer charges over a few angstroms, and many proteins possess large permanent dipoles to begin with; a *state change* at the tens-of-Debye level is therefore plausible. We adopt $\Delta p = 20 \text{ D}$ as a conservative, order-of-magnitude baseline [31].

The sensor consists of two $^{171}\text{Yb}^+$ ions with equilibrium separation $d \approx 3.45 \mu\text{m}$ (for an axial trap frequency $\omega_x = 2\pi \times 1 \text{ MHz}$). Interface effects of the vitrified film and the orientation distribution are treated explicitly below via the multiplicative factor η and an RMS projection factor, respectively.

a. *Numerical evaluation at $h = 10 \mu\text{m}$.* For $d/h = 0.345$, $c_{\text{eff}} \approx 2.79$. In vacuum ($\eta_{\perp} = 1$) this gives $\Delta E_{x,\text{max}} \approx 5.7 \times 10^{-4} \text{ V/m}$; including $\eta_{\perp} \approx 0.5$, $\Delta E_{x,\text{max}} \approx 2.9 \times 10^{-4} \text{ V/m}$.

Assuming an isotropic distribution of receptor orientations, we apply a conservative RMS projection factor of $1/\sqrt{3}$ for the detected Cartesian component,

$$\boxed{\Delta E_{\text{sig,RMS}}(h=10 \mu\text{m}) \approx \frac{1}{\sqrt{3}} \times 2.68 \times 10^{-4} \text{ V/m} \approx 1.55 \times 10^{-4} \text{ V/m}}. \quad (8)$$

b. *Scaling and a $30 \mu\text{m}$ reference point.* Because $\Delta E \propto d h^{-4}$ (Eq. 1), increasing the height from 10 to $30 \mu\text{m}$ reduces the signal by approximately $3^4 = 81$, with a small additional increase due to the mild growth of c_{eff} as d/h decreases. Numerically (lateral geometry, vacuum),

$$\Delta E_{x,\text{max}}(h = 30 \mu\text{m}, d = 3.45 \mu\text{m}) \approx 6.96 \times 10^{-6} \text{ V/m}.$$

Including the dielectric interface factor ($\eta \simeq 0.5$) and the same isotropic-projection factor $1/\sqrt{3}$,

$$\boxed{\Delta E_{\text{sig,RMS}}(h = 30 \mu\text{m}) \approx 2.0 \times 10^{-6} \text{ V/m}}.$$

We use these RMS values in the subsequent SNR analysis. The steep h^{-4} scaling highlights the importance of operating near $h \sim 10 \mu\text{m}$ and, where feasible, increasing the baseline d (e.g., via a double well) to linearly boost the signal.

C. Noise Analysis and Sensitivity Limits

The feasibility of the QLI depends critically on the dominant noise sources in the system. We must consider two distinct regimes: sensor-limited operation and sample-noise-limited operation.

1. Sensor-limited sensitivity (best case)

In the best case, the noise floor is determined by the intrinsic sensitivity of the ion gradiometer itself, assuming the electrostatic noise from the vitrified sample is negligible. We therefore anchor our estimates to experimentally realized low-frequency sensitivities in comparable single-ion electrometry, rather than extrapolating MHz-frequency surface-noise models.

Recent precision electrometry with single trapped ions reports the following noise-equivalent field sensitivities [28]:

- DC sensitivity (Hahn-echo): $S_{\text{DC}} \approx 1.97 \text{ mV m}^{-1}/\sqrt{\text{Hz}}$
- AC sensitivity (near 5.8 Hz): $S_{\text{AC}} \approx 0.96 \text{ mV m}^{-1}/\sqrt{\text{Hz}}$

While a two-ion entangled differential readout can ideally improve phase sensitivity by $\sqrt{2}$, we conservatively use the demonstrated single-ion values here.

Using the *lateral* two-ion geometry and incorporating (i) the dielectric-interface factor for amorphous ice, $\eta \simeq 2/(\epsilon_r+1) \approx 0.5$ with $\epsilon_r \approx 3$ [32], and (ii) an isotropic orientation RMS projection factor $1/\sqrt{3}$, the signal at $h = 10 \mu\text{m}$ evaluates to

$$\Delta E_{\text{sig,RMS}}(h=10 \mu\text{m}) \approx 1.55 \times 10^{-4} \text{ V/m.}$$

The corresponding sensor-limited performance is:

- $\text{SNR}_{\text{AC}}(1 \text{ s}) \approx \frac{1.55 \times 10^{-4}}{0.96 \times 10^{-3}} \approx 0.16$, $\tau_{\text{AC}}(\text{SNR}=1) \approx 38 \text{ s}$
- $\text{SNR}_{\text{DC}}(1 \text{ s}) \approx \frac{1.55 \times 10^{-4}}{1.97 \times 10^{-3}} \approx 0.08$, $\tau_{\text{DC}}(\text{SNR}=1) \approx 162 \text{ s}$

For $\text{SNR}=10$, these times scale by 100, giving ~ 64 minutes (AC) and ~ 4.5 hours (DC).

At a more conservative height of $h = 30 \mu\text{m}$ the signal scales as $\Delta E \propto d h^{-4}$, reducing the amplitude by ≈ 81 (with a small additional change from c_{eff}). Numerically,

$$\Delta E_{\text{sig,RMS}}(h=30 \mu\text{m}) \approx 2.0 \times 10^{-6} \text{ V/m,}$$

leading to

- $\tau_{\text{AC}}(\text{SNR}=1) \approx 63 \text{ h}$,
- $\tau_{\text{DC}}(\text{SNR}=1) \approx 11 \text{ days}$.

Baseline leverage (double well). Increasing the differential baseline from $d = 3.45 \mu\text{m}$ to $d = 10 \mu\text{m}$ reduces integration times by $(3.45/10)^2 \approx 0.12$:

$$\tau_{\text{AC}}(10 \mu\text{m}) \approx 4.5 \text{ s}, \quad \tau_{\text{DC}}(10 \mu\text{m}) \approx 19 \text{ s.}$$

(Additional gains are possible with a metal underlayer, $\eta \simeq 2$, or entangled differential readout; we omit these here to remain conservative.)

2. The critical unknown: sample noise

The analysis above assumes the noise floor is set by the sensor. The dominant risk is that the vitrified sample generates *differential* electric-field noise above the instrument floor in our measurement band [13].

a. Differential sample noise and correlation. Let $\mathcal{S}_E(f)$ denote the (single-point) electric-field noise PSD ($\text{V}^2 \text{ m}^{-2}/\text{Hz}$) from the sample at frequency f , and let $\mathcal{C}(f; d)$ be the spatial correlation between the two ion positions (baseline d). The *differential* field-noise PSD is

$$\mathcal{S}_E^{\text{diff}}(f) = 2 \mathcal{S}_E(f) [1 - \mathcal{C}(f; d)], \quad (9)$$

so the corresponding ASD is $s_{\text{sample}}(f) = \sqrt{\mathcal{S}_E^{\text{diff}}(f)}$ ($\text{V m}^{-1}/\sqrt{\text{Hz}}$). For correlation lengths $\ell \gg d$, $\mathcal{C} \rightarrow 1$ and the gradiometer cancels most sample noise; for $\ell \ll d$, $\mathcal{C} \rightarrow 0$ and the differential ASD is larger by $\sqrt{2}$. Spatial correlations with $\ell \sim 10^2 \mu\text{m}$ have been inferred in surface traps at tens–hundreds of microns [33, 34].

b. How sample noise combines with instrument sensitivity. Let s_{sens} be the instrument noise-equivalent field ASD of the electrometer protocol (e.g., $s_{\text{AC}} = 0.96 \text{ mV m}^{-1}/\sqrt{\text{Hz}}$, $s_{\text{DC}} = 1.97 \text{ mV m}^{-1}/\sqrt{\text{Hz}}$ [28]). The total differential ASD is

$$s_{\text{tot}}(f) = \sqrt{s_{\text{sens}}^2 + s_{\text{sample}}^2(f)}. \quad (10)$$

Integration time scales as $\tau \propto s_{\text{tot}}^2$, so the slow-down factor relative to the sensor-limited case is

$$\frac{\tau}{\tau_0} = 1 + \left(\frac{s_{\text{sample}}(f)}{s_{\text{sens}}} \right)^2.$$

To keep the penalty below 20% it suffices that $s_{\text{sample}}(f) \lesssim 0.45 s_{\text{sens}}$.

c. Sources and measurement plan. The vitrified sample (amorphous ice, proteins, buffer salts) is a complex dielectric at 4 K; plausible mechanisms include (i) two-level systems (TLS) in the amorphous matrix, which generically give $1/f$ -like spectra [35, 36], and (ii) slow charge/polarization relaxations of proteins and trapped ions. To our knowledge the differential field noise from vitrified biological matter at cryogenic temperature and $h \sim 10 \mu\text{m}$ has not been measured. We will therefore determine $s_{\text{sample}}(f)$ by (a) echo/lock-in measurements with the sample present vs. retracted, (b) sweeping d to estimate $\mathcal{C}(f; d)$ via Eq. (9), and (c) sweeping h to extract the distance exponent in our band [33, 34].

d. Mitigations if sample noise dominates. If $s_{\text{sample}}(f) \gtrsim s_{\text{sens}}$, one could (i) up-convert the signal using a small lateral dither (quantum lock-in) into a quieter band [29, 30], (ii) increase d (double well) to boost signal linearly while sample noise remains correlated across the baseline, and (iii) employ a metal underlayer beneath the vitrified film, which both increases signal for normal dipoles (image-dipole doubling, $\eta \simeq 2$) and can improve correlation across d [17].

D. Background Stability and the Path Forward

The QLI relies on subtracting a large, static background field gradient to isolate the small differential signal from ligand binding. This subtraction is only viable if the background is sufficiently stable over the averaging time (minutes to hours).

a. What “stable enough” means (quantitative target). Let s_{sens} denote the instrument noise-equivalent field ASD (e.g., $s_{\text{AC}} = 0.96 \text{ mV m}^{-1}/\sqrt{\text{Hz}}$, $s_{\text{DC}} = 1.97 \text{ mV m}^{-1}/\sqrt{\text{Hz}}$), and let $s_{\text{sample}}(f)$ denote the differential field-noise ASD from the sample (Eq. 10). To keep the integration-time penalty below 20%, we require

$$s_{\text{sample}}(f_0) \lesssim 0.45 s_{\text{sens}},$$

at the demodulation frequency f_0 (AC/lock-in) or within the echo bandwidth (DC). Numerically, this corresponds to $s_{\text{sample}}(5.8 \text{ Hz}) \lesssim 0.43 \text{ mV m}^{-1}/\sqrt{\text{Hz}}$ and $s_{\text{sample}}^{\text{DC}} \lesssim 0.88 \text{ mV m}^{-1}/\sqrt{\text{Hz}}$.

b. Precursor experiment (Milestone 3). Before biological detection, we will directly characterize the differential background with a *bare, vitrified* stylus:

1. Measure $\Delta E_x(t)$ at fixed (h, d) to obtain the PSD $s_{\text{sample}}(f)$ and the Allan deviation $\sigma_{\Delta E}(\tau)$; verify $s_{\text{sample}}(f_0)$ meets the above target.
2. Sweep h (e.g., $10 \rightarrow 30 \mu\text{m}$) to extract the distance exponent in our band.
3. Sweep d (e.g., $3.45 \rightarrow 10 \mu\text{m}$, double well) to estimate the spatial correlation $\mathcal{C}(f; d)$ via the differential PSD relation.
4. Calibrate common-mode rejection by applying a uniform reference field and reporting the common-mode rejection ratio (CMRR) of the gradiometer.

If $s_{\text{sample}}(f_0) \gtrsim s_{\text{sens}}$, we will (i) up-convert the signal with a small lateral stylus dither to a quieter f_0 (quantum lock-in), (ii) increase d (double well) to boost signal linearly while sample noise remains correlated across the baseline, and (iii) test a metal underlayer beneath the vitrified film, which increases signal for normal dipoles (effective $\eta \simeq 2$) and can improve correlation across d . These steps keep feasibility anchored to *measured* $s_{\text{sample}}(f)$.

E. Throughput and Scalability

The QLI is inherently low-throughput due to cryogenic operation, sample handling, and multi-minute integrations. A realistic per-site time budget is:

$$T_{\text{site}} \approx T_{\text{setup}} + T_{\text{align}} + T_{\text{cal}} + N_{\text{avg}} \times \tau(\text{SNR}),$$

with T_{setup} (stylus transfer/temperature stabilization), T_{align} (ion–stylus approach and centering), and T_{cal} (field/phase calibration).

Two representative operating points at $h = 10 \mu\text{m}$ (sensor-limited, Sec. III):

- **Baseline gradiometer ($d = 3.45 \mu\text{m}$):** $\tau_{\text{AC}}(\text{SNR} = 10) \approx 64$ minutes. With $T_{\text{setup}} + T_{\text{align}} + T_{\text{cal}} \sim 30\text{--}60$ minutes and $N_{\text{avg}} = 1\text{--}2$, this yields $\sim 1\text{--}3$ sites per day.
- **Double well ($d = 10 \mu\text{m}$):** $\tau_{\text{AC}}(\text{SNR} = 10) \approx 7.5$ minutes (factor ≈ 8.4 faster). Including overheads, $\sim 4\text{--}8$ sites per day.

Practical scalability levers include (i) a double-well baseline to reduce τ as $1/d^2$, (ii) scripted alignment/calibration to minimize overheads, and (iii) multi-zone traps to shuttle the ion pair between pre-vitrified sites without repositioning the stylus.

F. Fidelity of Sample Preparation and Measurement

Vitrification fidelity: The premise relies on vitrification faithfully preserving the ligand-bound state. While cryo-EM routinely utilizes this method, dissociation can be a concern for low-affinity binders during the blotting and freezing process. Initial experiments should therefore target high-affinity ligand–receptor pairs.

Measurement-induced heating and cooling: The laser pulses used to manipulate the ion spins and motional states (e.g., the SDF sequence) will inevitably cause some recoil

heating due to off-resonant photon scattering. The heating rate, Γ_{heat} , must be kept lower than the sympathetic cooling rate, Γ_{cool} , provided by the coolant ion (e.g., $^{40}\text{Ca}^+$). In mixed-species crystals, sympathetic cooling is very effective and generally sufficient to counteract the minimal heating from a well-tuned pulse sequence, ensuring the sensor ions remain deep within the Lamb–Dicke regime for the duration of the measurement.

IV. EXPERIMENTAL ROADMAP AND OUTLOOK

TABLE II. Proposed developmental milestones for the QLI.

Milestone	Objective	Key challenge
1. Gradiometer validation	Demonstrate gradient extraction using a metallic nano-tip with a calibrated voltage.	Achieving stable, low-noise operation of the two-ion gradiometer.
2. Ion–surface proximity	Characterize motional heating and stability while pushing from 30 μm toward 10–20 μm ; identify limits to further reduction.	Mitigating anomalous heating at close proximity.
3. Background characterization	Quantify the static field gradient and temporal drift from a bare vitrified buffer sample.	Determining if background stability is sufficient for signal subtraction.
4. Model system proof-of-principle	Detect the dipole change from a robust, well-characterized process (e.g., DNA hybridization).	Bridging quantum sensor with a simplified, yet realistic, biological sample.
5. First protein–ligand detection	Detect the electrostatic difference between the apo and holo states of a high-affinity receptor.	Achieving sufficient signal fidelity and background rejection.

The successful development of the QLI hinges on this phased approach, retiring key risks sequentially. A primary goal is to establish clear metrics for success beyond simple detection, focusing on the precision and reproducibility necessary to provide biologically relevant electrostatic data. While the architecture proposed here is ambitious, future research may also

explore alternative quantum sensors, such as nitrogen-vacancy centers in diamond, which could potentially mitigate the need for UHV/cryogenic environments, albeit with their own distinct challenges in sensitivity and surface proximity.

V. CONCLUSION

We presented a two-ion Ramsey gradiometer for label-free single-molecule *state* detection in cryogenic vacuum. In the surface-trap geometry (ions at equal height h with lateral baseline d), the differential signal from a normal dipole change scales as $\Delta E \propto \eta \Delta p d h^{-4}$ with an $\mathcal{O}(1)$ geometry factor. Anchored to measured low-frequency single-ion sensitivities [28] and using conservative interface/orientation factors, the expected signal from $\Delta p \sim 20$ D at $h \approx 10$ μm yields $\text{SNR} = 1$ in *tens of seconds*. Increasing d (e.g., a double well) provides a linear gain in signal, whereas operating at $h \approx 30$ μm is unattractive in the same regime due to the steep h^{-4} scaling.

The decisive unknown is the *differential* electric-field noise of vitrified samples. We set a quantitative gate for feasibility: $s_{\text{sample}}(f_0) \lesssim 0.45 s_{\text{sens}}$ at the demodulation frequency f_0 to keep integration-time penalties below 20%. Our immediate objective is therefore a precursor measurement of the sample’s noise spectrum and stability (PSD vs. f) together with distance and baseline sweeps (vs. h and d) to determine scaling and spatial correlation. If needed, mitigations include up-conversion (quantum lock-in), larger d , and metal underlayers that increase normal-dipole signals.

The QLI is low-throughput by design, but it targets a distinct niche: static, label-free electrostatic contrast between apo and holo states at the single-molecule level. Establishing the sample-noise landscape *in situ* will determine the optimal operating point (baseline, height, band) and provide the empirical foundation for bringing quantum metrology to electrostatics in biology.

- [1] H. A. Rockman and R. J. Lefkowitz, *Journal of Clinical Investigation* **134**, e178109 (2024).
- [2] S. Bobone, C. Storti, C. Fulci, A. Damiani, *et al.*, *The Journal of Physical Chemistry Letters* **15**, 10252 (2024).
- [3] J. Hellmeier, E. Ploetz, N. Dollenbacher, and T. Hügel, *Nano Letters* **19**, 7744 (2019).

- [4] J. Icha, M. Weber, J. C. Waters, and C. Norden, *BioEssays* **39**, 1700003 (2017).
- [5] X. Guo, *Sensors* **15**, 10481 (2015).
- [6] S. G. Boxer, *Journal of Physical Chemistry B* **113**, 2972 (2009).
- [7] A. K. Sinensky and A. M. Belcher, *Nature Nanotechnology* **2**, 653 (2007).
- [8] A. Warshel, P. K. Sharma, M. Kato, Y. Xiang, H. Liu, and M. H. M. Olsson, *Chemical Reviews* **106**, 3210 (2006).
- [9] S. D. Fried, S. Bagchi, and S. G. Boxer, *Science* **346**, 1510 (2014).
- [10] C. L. Degen, F. Reinhard, and P. Cappellaro, *Reviews of Modern Physics* **89**, 035002 (2017).
- [11] A. D. Ludlow, M. M. Boyd, J. Ye, E. Peik, and P. O. Schmidt, *Reviews of Modern Physics* **87**, 637 (2015).
- [12] M. J. Biercuk, H. Uys, J. W. Britton, A. P. VanDevender, and J. J. Bollinger, *Nature Nanotechnology* **5**, 646 (2010).
- [13] M. Brownnutt, M. Kumph, P. Rabl, and R. Blatt, *Reviews of Modern Physics* **87**, 1419 (2015).
- [14] K. A. Gilmore, M. Affolter, R. J. Lewis-Swan, D. Barberena, E. Jordan, A. M. Rey, and J. J. Bollinger, *Science* **373**, 673 (2021).
- [15] J. F. Barry, M. J. Turner, J. M. Schloss, D. R. Glenn, Y. Song, M. D. Lukin, H. Park, and R. L. Walsworth, *Proceedings of the National Academy of Sciences* **113**, 14133 (2016).
- [16] J. Yoo, H. Kim, Y. Kim, and T. Choi, *Nano Convergence* **12**, 12 (2025).
- [17] J. D. Jackson, *Classical Electrodynamics*, 3rd ed. (Wiley, New York, 1998).
- [18] D. Leibrandt, B. Yurke, and R. Slusher, *Quantum Information and Computation* **7**, 52 (2007).
- [19] K. Mølmer and A. Sørensen, *Phys. Rev. Lett.* **82**, 1835 (1999).
- [20] D. Kielpinski, V. Meyer, M. A. Rowe, C. A. Sackett, W. M. Itano, C. Monroe, and D. J. Wineland, *Science* **291**, 1013 (2001).
- [21] R. Blatt and D. Wineland, *Nature* **453**, 1008 (2008).
- [22] D. Leibfried, B. DeMarco, V. Meyer, D. Lucas, M. Barrett, J. Britton, W. M. Itano, B. Ježenković, C. Langer, T. Rosenband, and D. J. Wineland, *Nature* **422**, 412 (2003).
- [23] T. Ruster, H. Kaufmann, M. A. Luda, V. Kaushal, C. T. Schmiegelow, F. Schmidt-Kaler, and U. G. Poschinger, *Physical Review X* **7**, 031050 (2017).
- [24] A. H. Myerson, D. J. Szwarc, S. C. Webster, D. T. C. Allcock, M. J. Curtis, G. Imreh, J. A. Sherman, D. N. Stacey, A. M. Steane, and D. M. Lucas, *Phys. Rev. Lett.* **100**, 200502 (2008).
- [25] J. Dubochet, M. Adrian, J.-J. Chang, J.-C. Homo, J. Lepault, A. W. McDowall, and P. Schultz,

Quarterly Reviews of Biophysics **21**, 129 (1988).

- [26] R. Maiwald, D. Leibfried, J. Britton, J. C. Bergquist, G. Leuchs, and D. J. Wineland, Nature Physics **5**, 551 (2009).
- [27] M. Harlander, M. Brownnutt, W. Hänsel, and R. Blatt, New Journal of Physics **12**, 093035 (2010).
- [28] F. Bonus, C. Knapp, C. H. Valahu, J. F. Goodwin, R. C. Thompson, and T. P. Harty, Nature Physics (2025).
- [29] S. Kotler, N. Akerman, Y. Glickman, A. Keselman, and R. Ozeri, Nature **473**, 61 (2011).
- [30] J. Bylander, S. Gustavsson, F. Yan, F. Yoshihara, K. Harrabi, G. Fitch, D. G. Cory, Y. Nakamura, J.-S. Tsai, and W. D. Oliver, Nature Physics **7**, 565 (2011).
- [31] Z. Zhang, S. Witham, and E. Alexov, Physical Biology **8**, 035001 (2011).
- [32] G. P. Johari, A. Hallbrucker, and E. Mayer, Science **273**, 90 (1996).
- [33] D. An, C. Matthiesen, E. Urban, and H. Häffner, Physical Review A **100**, 063405 (2019).
- [34] J. A. Sedlacek, J. Stuart, J. Hannegan, C. D. Bruzewicz, R. McConnell, and J. M. Sage, Physical Review A **97**, 053406 (2018).
- [35] W. A. Phillips, Reports on Progress in Physics **50**, 1657 (1987).
- [36] P. Dutta and P. M. Horn, Reviews of Modern Physics **53**, 497 (1981).